Received September 1998
Revised January 2000
Accepted January 2000

3D numerical simulation of melt flow in the presence of a rotating magnetic field

D. Vizman
Department of Physics, West University of Timisoara,
Timisoara, Romania
B. Fischer
Institute for Materials Science WW VI, University Erlangen-Nürnberg,
Erlangen, Germany,
J. Friedrich and G. Müller
Fraunhofer Institute for Integrated Circuits IIS-B, Erlangen, Germany

Keywords *Magnetic fields, Numerical simulation, 3D, Flow, Melting*

Abstract *Being extensively used in metallurgy, rotating magnetic fields are also becoming increasingly interesting for application in crystal growth, where they are intended to act by stabilizing the melt flow. For this purpose, it is important to understand the basic interactions of the magnetically induced flow and other flow components like time-dependent buoyant convection. So a three-dimensional finite volume method was developed in order to numerically study the effect of a rotating magnetic field on convection in a cylindrical melt volume. The equations of mass, momentum, and heat transport are solved together with the potential equations describing the electromagnetic field. The numerical computation of the Lorenz force distribution is validated by comparison with an analytical solution. The effects of magnetic field parameters on the temperature distributions and the flow patterns in the considered configurations are analysed.*

1. Introduction

The flow in electrically conducting melts, like metals or semiconductors, can be contactlessly influenced by externally applied magnetic fields. In metallurgy, various kinds of magnetic fields have been in use for decades, e.g. for the mixing of alloys or controlling the melt flow in continuous casting of steel (Spitzer *et al.*, 1986). Industrial semiconductor crystal growth from the melt has included the application of magnetic fields only for about the last two decades. Nevertheless, the damping of undesirable flow components resulting from buoyancy by steady magnetic fields is well-established, for example, in the growth of silicon crystals by the Czochralski method (Müller, 1998). In this way, inhomogeneities in the grown crystal can be sufficiently suppressed. However, this often requires large magnetic field strengths and thus large and expensive magnets. In Tomzig *et al.* (1999), a facility for generating a 0.15 T static cusp field (Müller, 1998) is said to have a weight of 10 tons and an energy consumption of 400kW. For large melt volumes – industrial Czochralski crucibles may have diameters of 32 inches – the necessary magnetic induction is in the range of several tesla. This is why the possibilities of time-dependent, e.g. rotating, magnetic fields have been the focus of academic and industrial interest in recent years. Their use requires significantly lower magnetic inductions and they can thus be realised by relatively simple coil arrangements. Time-dependent magnetic fields do not damp selected flow components like steady magnetic fields, but enforce a certain flow direction, thus suppressing other disturbing flow components. In the case of a magnetic field rotating in the horizontal plane around the vertical axis, a Lorentz force in dominantly azimuthal direction is induced, resulting in a forced fluid flow in azimuthal direction again. This basically means that the fluid is stirred and shows a rotational motion. Solid end walls of the container result in an additional secondary motion in the meridional plane. The optimizing and development of magnetic facilities for crystal growth for both static and time-dependent magnetic fields are an important aspect of competition among the semiconductor producers. In order to improve the usefulness of time-dependent – in our case rotating – magnetic fields for industrial applications, it is important to understand the basic mechanisms of the interaction of the magnetically induced flow and other flow components like buoyancy, as well as to carry out extensive parameter studies in model configurations.

Significant literature on the application of rotating magnetic fields can be found even in the 1960s (Johnston and Tiller, 1961). A lot of theoretical work on the action of a rotating magnetic field on a conducting liquid has been done, including manifold analytical solutions and flow stability analyses (Moffatt, 1965, 1978; Richardson, 1974; Davidson, 1992). In many cases, simplified configurations are considered like infinite cylinders as approximation for long finite cylindrical containers. More realistic analytical approaches for the flow in finite cylinders can be found, e.g. in Gelfgat *et al.* (1993) and Gorbunov and Kolevzon (1993). A very detailed survey on the early theoretical work is given in Dahlberg (1972), while Gelfgat and Priede (1995) give an up-to-date summary on rotating magnetic field studies up to 1995. A first numerical model for finite cylinders with electrically insulating walls was presented in Gelfgat *et al.* (1991) and Priede (1993), including basic flow regime analysis. In Priede and Gelfgat (1997) an extended study was presented, investigating the influence of conducting walls and identifying the generation of Taylor-vortex-type instabilities at the vertical cylinder wall, which are carried to the cylinder end walls by the meridional secondary convection. The effects of a finite magnetic inductor and its position relative to the melt, as well as the influence of two counter-rotating magnetic fields, were studied in Abricka *et al.* (1997). A parameter study for field frequency and amplitude was presented in Barz *et al.* (1997). Kaiser (1998) also made a numerical stabilty analysis for a cylinder, investigating the influence of aspect ratio on the generation of the Taylor-type vortices. A study of stability thesholds and the superposition of steady and rotating magnetic fields can be found in Mößner and Gerbeth (1999).

All of these numerical studies deal with 2D models, assuming axial symmetry. Basically, this is only justified as long as there is the mere rotation induced by the magnetic field and no other or only very weak three-dimensional time-dependent flow components like buoyant convection. Therefore, the numerical work mentioned above mainly considers isothermal melts or a temperature profile resulting in a stable layering of the fluid. In Kaiser (1998) also a Bénard configuration was considered, but the Rayleigh number was chosen such that no buoyancy convection develops. Mößner and Gerbeth (1999) also investigated buoyant convection in axial symmetry for heated side walls.

Only very few simulations have been done with a 3D model, which, however, is necessary to correctly seize the interaction of magnetic and buoyant forces. In former studies by our group (Fischer *et al.*, 1997; Friedrich *et al.*, 1999) 3D time-dependent numerical simulations were carried out for a cylinder with aspect ratio 1.0 and Rayleigh-Bénard temperature boundary conditions; i.e. a linear temperature profile with hot bottom and cold top was prescribed at the container walls. Concurrently, temperature measurements were made in a corresponding test cell filled with liquid gallium. It was found that temperature fluctuations resulting from time-dependent buoyant convection can be efficiently damped by applying a sufficient rotating magnetic field. With a smaller magnetic field regular sinusoidal temperature fluctuations indicate the precession of flow and temperature patterns that are a hybrid of meridional buoyant patterns and the magnetically forced rotation. This behaviour was confirmed in 3D simulations by Kaiser (1998). When increasing the magnetic field beyond the optimum value for damping, irregular high-frequency temperature fluctuations occur resulting from Taylor-vortex-type instabilities. All these flow regimes were also found in the experiments, showing a good accordance with the numerical results. Another detailed experimental analysis of flow regimes was done by Volz and Mazuruk (1996).

In this paper, we put the emphasis on introducing the method for the numerical treatment of the rotating magnetic field, which is explained in detail. The numerical calculations of the Lorentz force are compared to analytical solutions for the case without taking into account fluid flow. Furthermore, we present new results of 3D numerical simulations of melt convection under the action of a rotating magnetic field in a finite cylindrical volume with aspect ratio 0.5, which are a continuation of the numerical studies in Friedrich *et al.* (1999) for aspect ratio 1.0. In this work, former observations are confirmed and some additional flow regimes revealed.

2. Model description

2.1 Governing equations

The melt flow is governed by the three-dimensional equations describing mass, momentum, and heat transport. In a Cartesian coordinate system (y_1, y_2, y_3), making use of the Boussinesq approximation for an incompressible fluid $(f_{g,i} = -\rho(T_{\mathrm{ref}})\, g_i\, \beta(T - T_{\mathrm{ref}}))$ and of an additional term for the Lorentz force density $(f_{L,i} = (\vec{j} \times \vec{B})_i)$ to take into account the magnetic field, we have the following set of magnetohydrodynamic equations:

$$\frac{\partial}{\partial y_i}(\rho u_i) = 0 \qquad (1)$$

$$\frac{\partial}{\partial t}(\rho u_i) = -\frac{\partial}{\partial y_j}\left(\rho u_i u_j + \tau_{ij}\right) - \frac{\partial p}{\partial y_i} + f_{g,i} + f_{L,i} \tag{2}$$

$$\frac{\partial}{\partial t}(\rho T) = -\frac{\partial}{\partial y_j}\left(\rho u_j T - \Gamma_T \frac{\partial T}{\partial y_j}\right) \tag{3}$$

Thereby ρ is the density, u_i is the i-th Cartesian component of the melt velocity (i = 1,2,3), p is the pressure, Γ_T is the diffusion coefficient for the temperature, T_{ref} is a reference temperature, g_i is the i-th component of the gravitational acceleration, β is the thermal expansion coefficient, τ_{ij} is the stress tensor, $\vec{B}$ is the magnetic induction and $\vec{j}$ is the current density.

For an incompressible Newtonian fluid with dynamic viscosity μ, the stress tensor is defined as:

$$\tau_{ij} = -\mu\left(\frac{\partial u_i}{\partial y_j} + \frac{\partial u_j}{\partial y_i}\right) \tag{4}$$

The current density $\vec{j}$ is determined by Ohm's law

$$\vec{j} = \sigma\left(\vec{E} + \vec{u} \times \vec{B}\right), \tag{5}$$

with σ representing the electrical conductivity.

The electric field $\vec{E}$ can be written in terms of the electrodynamic potentials (see Moreau, 1990)

$$\vec{E} = -\vec{\nabla}\Phi - \frac{\partial \vec{A}}{\partial t}, \tag{6}$$

where $\vec{A}$ is the magnetic vector potential and Φ is the electric scalar potential. The continuity equation for the current density

$$\vec{\nabla} \cdot \vec{j} = 0 \tag{7}$$

yields the governing equation for the scalar potential Φ.

No-slip velocity boundary conditions and Dirichlet thermal boundary conditions are imposed on the walls of the melt container. The normal component of the electric current is assumed to be zero at the electrically insulating boundaries of the cylinder:

$$\vec{j} \cdot \vec{n} = 0 \tag{8}$$

2.2 Rotating magnetic field

For a cylindrical cavity of radius R, the externally applied rotating magnetic field $\vec{B}(y_1, y_2, y_3)$ (in this study with two pole pairs) can be written as:

$$\vec{B} = \left\{ -\frac{B_0}{R}(y_1 \sin \omega t - y_2 \cos \omega t);\ \frac{B_0}{R}(y_1 \cos \omega t + y_2 \sin \omega t);\ 0 \right\} \tag{9}$$

The corresponding magnetic vector potential can be easily obtained via $\vec{B} = \vec{\nabla} \times \vec{A}$ and the Coulomb gauge$\vec{\nabla} \cdot \vec{A} = 0$

$$\vec{A} = \left\{ 0;\ 0;\ -\frac{B_0}{2R}\left[(y_1^2 - y_2^2) \cos \omega t + 2 y_1 y_2 \sin \omega t \right] \right\}, \tag{10}$$

where B_0 is the magnetic field amplitude at radius R and $\frac{\omega}{2\pi}$ its frequency (for the case of two pole pairs, the rotation frequency of the magnetic field pattern is $\frac{\Omega}{2\pi} = \frac{1}{2}\frac{\omega}{2\pi}$). Using moderate frequencies, for which the skin depth $\delta = \sqrt{\frac{2}{\mu \sigma \omega}}$($\mu$: magnetic permeability) is not significantly smaller than the dimensions of our melt, we do not need to take into account the skin effect in our calculations (Moreau, 1990). One characteristic for this approximation is that there will be no phase shift between the rotating quantities. We can split the scalar potential Φ into Φ_1 and Φ_2 (Barz *et al.*, 1997), where:

$$\Phi = \Phi_1(y_1, y_2, y_3) \sin \omega t + \Phi_2(y_1, y_2, y_3) \cos \omega t \tag{11}$$

Together with equation (11) introduced in equations (6) and (5), equation (7) yields the governing equations for Φ_1 and Φ_2:

$$\Delta \Phi_{1,2} + \vec{\nabla} \cdot \vec{X}_{1,2} = 0\,, \tag{12}$$

where

$$\vec{X}_1 = \frac{B_0}{R}\{ y_2 u_3;\ y_1 u_3;\ y_2 u_1 + y_1 u_2 \} \tag{13}$$

$$\vec{X}_2 = \frac{B_0}{R}\{y_1u_3;\ -y_2u_3;\ -y_1u_1 + y_2u_2\} \tag{14}$$

At the boundary (see equation 8) we have:

$$\vec{n}\cdot\vec{\nabla}\Phi_1 = \vec{n}\cdot\left\{0;\ 0;\ \frac{\omega B_0}{2R}(y_2^2 - y_1^2)\right\} \tag{15}$$

$$\vec{n}\cdot\vec{\nabla}\Phi_2 = \vec{n}\cdot\left\{0;\ 0;\ \frac{\omega B_0}{R}y_2y_1\right\} \tag{16}$$

If $\vec{B}$ is changing with frequency ω, the quantities $\vec{E}$, $\vec{j}$, and Φ will change with the same frequency. Consequently, the Lorentz force consists of a mean time-independent part and an oscillating part. In the present work, we assume that due to its high inertia the fluid is unable to follow this oscillating force component. Therefore, our numerical analysis is limited to the time-independent mean Lorentz force.

The following integration leads to the time-averaged Lorentz force components:

$$\left\langle \vec{f}_L \right\rangle = \left(\frac{2\pi}{\omega}\right)^{-1}\int_0^{\frac{2\pi}{\omega}} \vec{j}\times\vec{B}\,dt \tag{17}$$

2.3 Numerical discretization method

The present simulations were done with the non-commercial finite volume code STHAMAS3D, which was developed in our group. It allows three-dimensional time-dependent simulations on a block-structured numerical grid. The code solves the governing equations (1-3) and (12) and is used on a Linux PC. Time-dependence and three dimensions coupled with extensive parameter variations require a large computational capacity and result in long computation times. So, for the more recent studies a vectorized version of the code was developed to be used on a Fujitsu VPP700 and a Cray T90 high performance computer.

The discretization procedure of the finite volume method (FVM) is well-known from its application to fluid flows (Perić, 1985; Leister, 1994; Ferziger and Perić, 1996). In our case,the method was extended to solve the magnetohydrodynamic equations (1-3) coupled with the scalar potential equation (12). The computational domain is a cylindrical cavity with height *H* and diameter *D*, which is subdivided into five blocks consisting of control volumes (CVs). The basic structure of the numerical grids used for the cylinders is illustrated in Figure 1. The grids are three-dimensional, structured, and non-orthogonal.

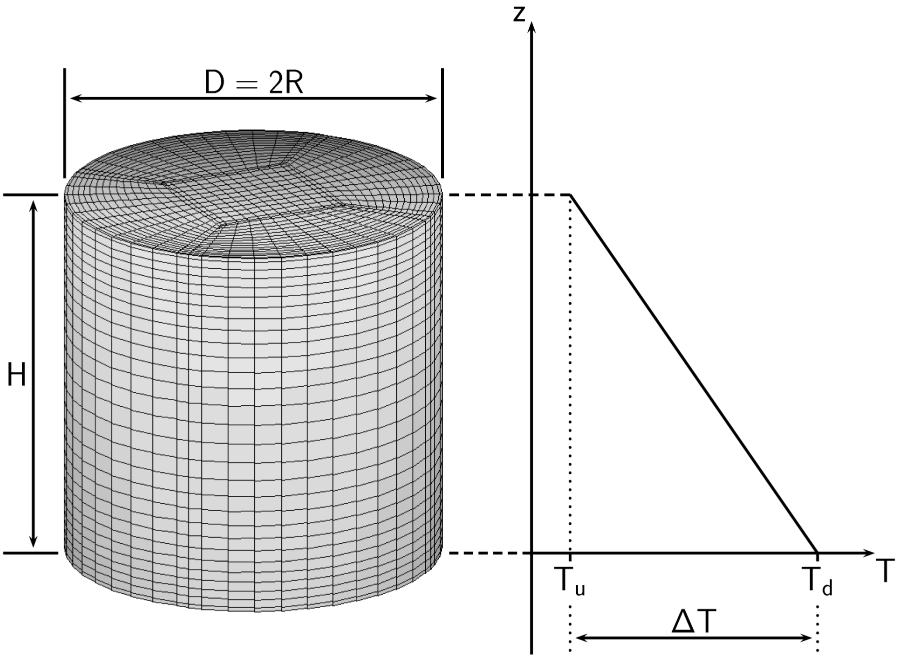

Figure 1.
The geometry of the cylindrical melt volume – with isothermal end plates (T_u and T_d) and a linear temperature profile along the side wall – and an illustration of the block-structured grid

An important issue for the quality of the numerical simulations is the choice of the grid. In this connection both the numerical resolution and the internal structure of the grid are crucial. The second item can be seen in the refining of the grid towards the walls of the melt container, which is necessary to properly resolve the boundary layers of the flow. A detailed grid size analysis presented in a former study by the authors (Friedrich *et al.*, 1999) showed 60,000 CVs to be completely sufficient for the considered flows in cylinders with aspect ratio $\frac{H}{D} = 1.0$. In addition, when keeping the diameter the necessary number of control volumes is approximately linearly dependent on the height of the cylinder. The use of the vectorized version of the code on high performance computers allowed us to choose a grid of 130,000 CVs for the latest studies of cylinders with aspect ratio $\frac{H}{D} = 0.5$ presented in this paper. Consequently, with such a grid the numerical resolution of all flow properties is absolutely ensured. As we have seen, the governing equation (12) for Φ_1 and Φ_2 has the following form:

$$\Delta\Phi + \vec{\nabla} \cdot \vec{X} = 0 \tag{18}$$

For the FVM it is necessary to have the integral formulation of the governing equations. Considering an arbitrary CV with volume V bounded by the surface S, equation (18) can be transformed by means of Gauss's theorem:

$$\int_V \left(\Delta\Phi + \vec{\nabla} \cdot \vec{X} \right) dV = \int_S \left(\vec{\nabla}\Phi + \vec{X} \right) \cdot d\vec{S} = 0 \tag{19}$$

Leaving the usual FVM neighbour nomenclature of E(ast), W(est), N(orth), S(outh), T(op) and B(ottom) (Figure 2) for reasons of convenience, the six faces of our CV are simply denoted by F_j ($j \in \{1,2,3,4,5,6\}$). The total surface S is equal to $S = \sum_j F_j$. Equation 20 can then be expressed by:

$$\sum_j \int_{F_j} (\vec{\nabla}\Phi + \vec{X}) \cdot d\vec{S} = 0 \tag{20}$$

It is known from Perić (1985), Leister (1994) and Ferziger and Perić (1996) that for a simple Laplace equation, the FVM yields a system of linear equations:

$$a_P \Phi_P = \sum_j a_j \Phi_j + S_\Phi\,, \tag{21}$$

where Φ_P denotes the value of Φ in the central point P of the CV and the Φ_j denote the values of Φ in the central points of the neighbouring CVs corresponding to the cell faces F_j. The a_j are the coefficients and S_Φ is the source term for the system. The a_j coefficients fulfill the relation $a_P = \sum_j a_j$. For more details, see Perić (1985), Leister (1994) and Ferziger and Perić (1996).

By applying the FVM to equation (20) one can obtain a system of equations similar to equation 21:

$$a_P \Phi_P = \sum_j a_j \Phi_j + S'_\Phi\,, \tag{22}$$

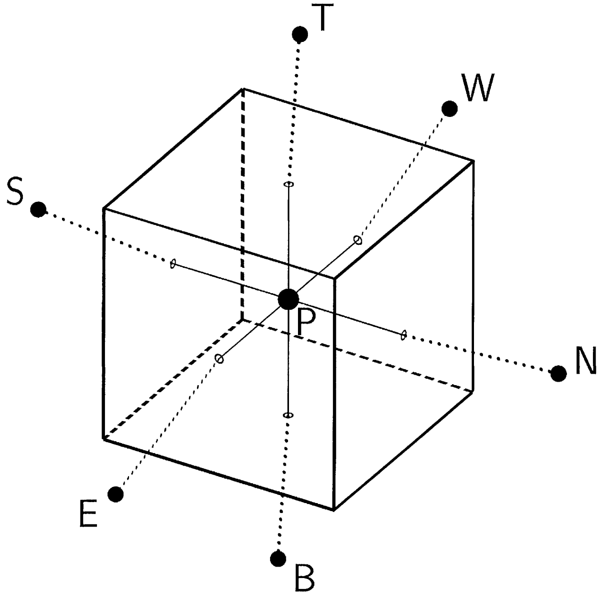

Figure 2.
Common finite volume nomenclature for a 3D control volume with the reference point P and its neighbouring points (E, W, N, S, T, B)

where

$$S'_{\Phi} = S_{\Phi} + \sum_{i,j} F^i_j X^i_j \,, \tag{23}$$

with F^i_j representing the i-component of the vector normal to the cell face F_j, and X^i_j representing the i-component of $\vec{X}$ on F_j ($i \in \{1,2,3\}$ and $j \in \{1,2,3,4,5,6\}$). By inserting equations (6), (9), (10) in equation (5) and finally using equation (17), the time-averaged Lorentz force components come out as:

$$\begin{aligned}
f_{L,1} &= \frac{\sigma B_0}{2R}\left[\frac{\partial\Phi_1}{\partial y_3}y_2 + \frac{\partial\Phi_2}{\partial y_3}y_1 - \frac{B_0\omega y_2 y_1^2}{2R} - \frac{B_0\omega y_2^3}{2R} - \frac{B_0 u_1 y_1^2}{R} - \frac{B_0 u_1 y_2^2}{R}\right]\\
f_{L,2} &= \frac{\sigma B_0}{2R}\left[\frac{\partial\Phi_1}{\partial y_3}y_1 - \frac{\partial\Phi_2}{\partial y_3}y_2 + \frac{B_0\omega y_1 y_2^2}{2R} + \frac{B_0\omega y_1^3}{2R} - \frac{B_0 u_2 y_1^2}{R} - \frac{B_0 u_2 y_2^2}{R}\right]\\
f_{L,3} &= \frac{\sigma B_0}{2R}\left[-\frac{\partial\Phi_1}{\partial y_1}y_2 - \frac{\partial\Phi_1}{\partial y_2}y_1 - \frac{\partial\Phi_2}{\partial y_1}y_1 + \frac{\partial\Phi_2}{\partial y_2}y_2 - \frac{2B_0 u_3 (y_1^2 + y_2^2)}{R}\right]
\end{aligned} \tag{24}$$

If no magnetic field is present, the FVM also yields a linear system of equations for the momentum equation (2) (see again Perić, 1985; Leister, 1994; Ferziger and Perić, 1996):

$$a_P u^P_i = \sum_j a_j u^j_i + S_{u_i} \,, \tag{25}$$

with u^j_i representing the i-th velocity component on the cell face F_j. If equation (24) is introduced in equation (2) and the FVM is applied, equation (25); becomes:

$$a'_P u^P_i = \sum_j a_j u^j_i + S'_{u_i} \,, \tag{26}$$

where the terms denoted by $'$ have the following meaning, e.g. for the first velocity component u_1:

$$\begin{aligned}
a'_P &= a_P + \frac{\sigma B_0^2 V(P)}{2R^2}\left[y_1^2 + y_2^2\right]\\
S'_{u_1} &= S_{u_1} + \frac{\sigma B_0 V(P)}{2R}\left[\frac{\partial\Phi_1}{\partial y_3}y_2 + \frac{\partial\Phi_2}{\partial y_3}y_1 - \frac{B_0\omega y_2 y_1^2}{2R} - \frac{B_0\omega y_2^3}{2R}\right]
\end{aligned} \tag{27}$$

where $V(P)$ is the volume of the CV P. The partial derivatives in equations (24) and (27) are numerically treated according to the finite volume method (Perić, 1985).

Similar relations can be obtained for the remaining two velocity components. The resulting set of algebraic equations is solved by the Strongly Implicit Method of Stone (Stone, 1968; Leister and Perić, 1994). The SIMPLE algorithm is applied for pressure correction (Patankar, 1980) and the Implicit Euler Method is made use of for time integration (Leister, 1994).

3. Results and discussions

3.1 Numerical calculations and analytical solutions

We have chosen a typical Rayleigh-Bénard configuration as test case. Our geometry is a cylinder with height H and diameter D. At the cylinder wall a linear temperature profile with a temperature difference $\Delta T = T_d - T_u$ is imposed (see Figure 1). Simulations were carried out for a gallium melt ($\rho = 6.1 \cdot 10^3 \frac{\mathrm{kg}}{\mathrm{m}^3}$, $\beta = 1.26 \cdot 10^{-4} K^{-1}$, $\mu = 1.907 \cdot 10^{-3} \frac{\mathrm{kg}}{\mathrm{ms}}$, $\Gamma_T = 9.22 \cdot 10^{-2} \frac{\mathrm{kg}}{\mathrm{ms}}$, and $\sigma = 3.87 \cdot 10^6 \frac{\mathrm{A}}{\mathrm{Vm}}$ (see Baumgartl, 1992).

If we do not take into account fluid flow ($\vec{u} = 0$), the equations for the scalar potential can also be solved analytically for a finite cylinder of radius R. In this case, the analytical solution for the Lorentz force density is:

$$f_{L,1} = f_\varphi \sin\varphi\,, \quad f_{L,2} = f_\varphi \cos\varphi\,, \quad f_{L,3} = 0\,, \tag{28}$$

where

$$f_\varphi = \sigma B_0^2 r\omega \left[\frac{1}{4}\left(\frac{r}{R}\right)^2 - \frac{1}{2}\sum_n \frac{J_2(\lambda_n \frac{r}{R}) J_3(\lambda_n)}{(J_2^2(\lambda_n) - J_1(\lambda_n)J_3(\lambda_n))\,\lambda_n} \left(\cosh\left(\lambda_n \frac{y_3}{R}\right) + \frac{(1-\cosh(\lambda_n \frac{H}{R}))}{\sinh(\lambda_n \frac{H}{R})} \sinh\left(\lambda_n \frac{y_3}{R}\right) \right) \right],$$

and $r = (y_1^2 + y_2^2)^{\frac{1}{2}}$ and φ come from the corresponding cylindrical coordinates $(r, \varphi, z = y_3)$.

J_p are the Bessel functions and λ_n are solutions of the equation

$$2\frac{J_2(x)}{x} - J_3(x) = 0\,.$$

See, for example, Gelfgat *et al.* (1993) for similar considerations with one pole pair.

In order to validate our numerical method we have carried out the numerical calculation of the Lorentz force for a cylinder with $H = 4$cm and $D = 4$cm, i.e. aspect ratio $\frac{H}{D} = 1.0$, without taking into account fluid flow ($\vec{u} = 0$). In our calculations we used $B_0 = 3.3$mT and ω =50Hz. The analytical solution was found using equation (28). A comparison of the numerical and analytical solutions for the azimuthal Lorentz force is given in Figures 3 and 4. Figure 3 shows the azimuthal Lorentz force along the $z = y_3$-axis at $r \approx \frac{3}{4}R$ and Figure 4 in radial direction at $z = y_3 = \frac{H}{2}$. It can be pointed out that the numerical and analytical results are in very good agreement.

3.2 Influence of rotating magnetic field on the flow

This paragraph is devoted to the results of a systematic numerical investigation of the action of the rotating magnetic field on the melt flow in a cylindrical Rayleigh-Bénard configuration as described in section 3.1. Calculations have been made for cylinders with aspect ratio 1.0 and 0.5, extensively varying several system parameters like the amplitude of the magnetic field and the thermal

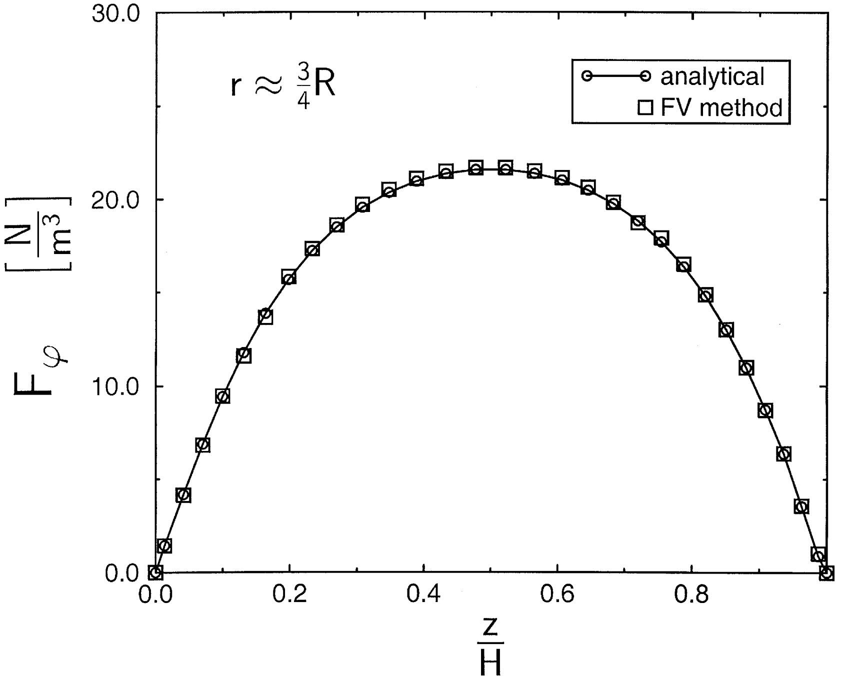

Figure 3.
Comparison of analytical and numerical values of the azimuthal Lorentz force along the z-axis (y_3-axis) at $r \approx \frac{3}{4}R$

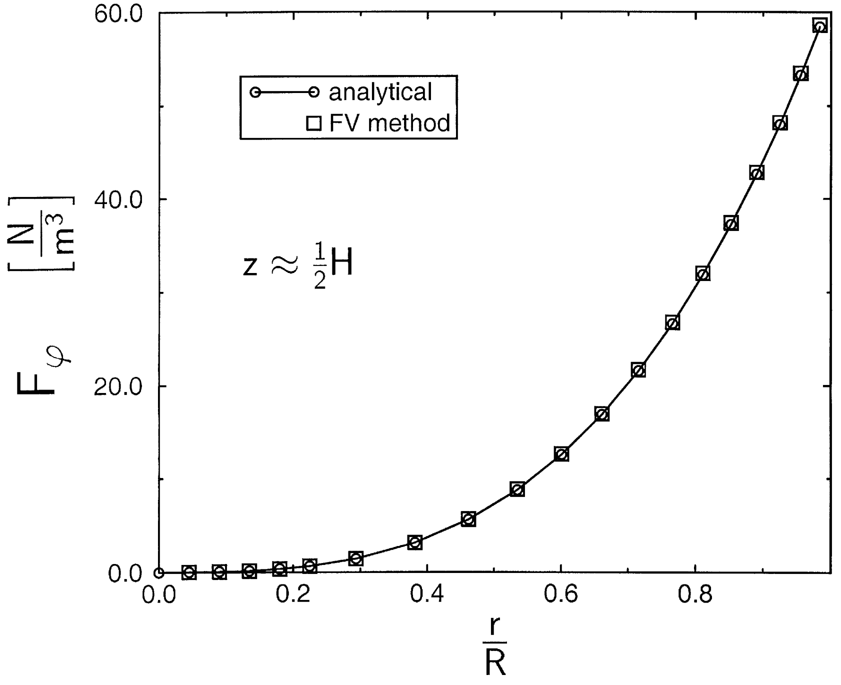

Figure 4.
Comparison of analytical and numerical values of the azimuthal Lorentz force in radial direction at $z = y_3 = \frac{H}{2}$

boundary conditions ΔT. Aspect ratio 1.0 (see section 3.1) has been studied in detail both numerically and experimentally in Fischer *et al.* (1997) and Friedrich *et al.* (1999), and we will only give a short retrospective description of that work. Taking a closer look at the latest numerical results for aspect ratio 0.5 (with $H = 1.7$cm, $D = 3.4$cm), the different flow regimes discovered will be explained in detail and compared to the ones identified for aspect ratio 1.0. Figure 5 illustrates the principal effect of a rotating magnetic field on fluid flow in a cylindrical melt (aspect ratio 1.0, $B_0 = 2.5$mT, $\omega = 2\pi\cdot$ 50Hz, ΔT=10K). The main flow, driven by the Lorentz force, is in the azimuthal direction, while being mainly in the meridional plane in the purely buoyant case (see, for example, Fischer *et al.*, 1997). The presence of the solid cylinder ends causes a secondary motion – two tori at the bottom and top of the melt, respectively (Figure 5b) – in the meridional plane, which is significantly smaller than the azimuthal rotation. The flow is basically axisymmetric. The isotherms in a vertical section are almost flat in the presence of the rotating magnetic field, which implies a stabilized heat and mass transport in the axial direction.

The change in the temperature profile can also be seen in Figure 6, where numerical and experimental values for the normalized temperature along the cylinder axis are plotted (Friedrich *et al.*, 1999), both for pure buoyancy and for a rotating magnetic field of 3.3mT (aspect ratio 1.0, $\omega = 2\pi\cdot$ 50Hz, ΔT=20K). There is a linearization of the temperature profile in the core of the melt due to the action of the magnetic field. The numerical results in Figure 6 agree qualitatively very well with the measurements. The quantitative deviations, especially for the case $B_0 = 0$mT, are mainly a consequence of experimental

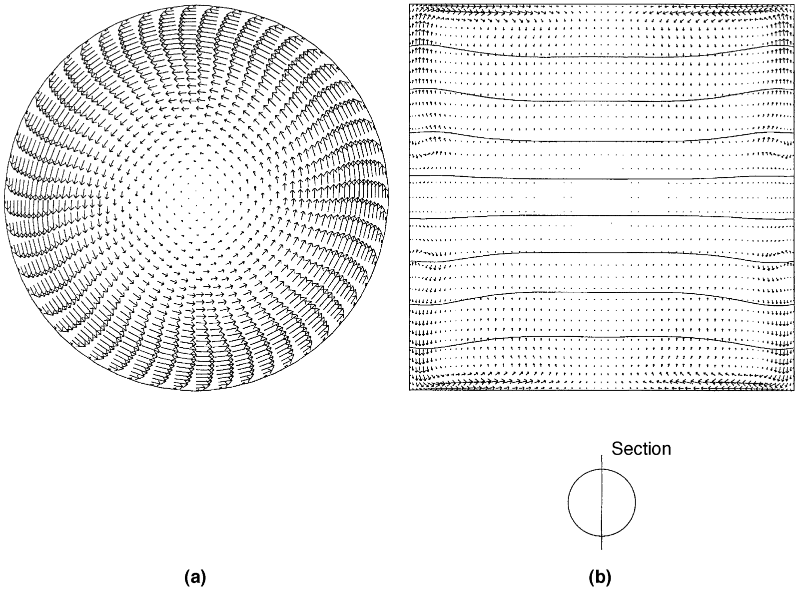

Source: Friedrich *et al.* (1999)

Figure 5.
Velocity profile and isotherms for the aspect ratio 1.0 Rayleigh-Bénard configuration with ΔT =10K in a horizontal (a), at $z = y_3 = \frac{H}{2}$, and vertical (b) section, with a rotating magnetic field (B_0 = 2.5mT, $\omega = 2\pi\cdot$ 50Hz). The isotherms are equally spaced (ΔT_{iso} = 1.1K). The maximum values of the cylindrical velocity components are: $v_{r,\max} = 7\,\frac{\mathrm{mm}}{s}$, $v_{\varphi,\max} = 22\,\frac{\mathrm{mm}}{\mathrm{s}}$, $v_{z,\max} = 3\,\frac{\mathrm{mm}}{s}$

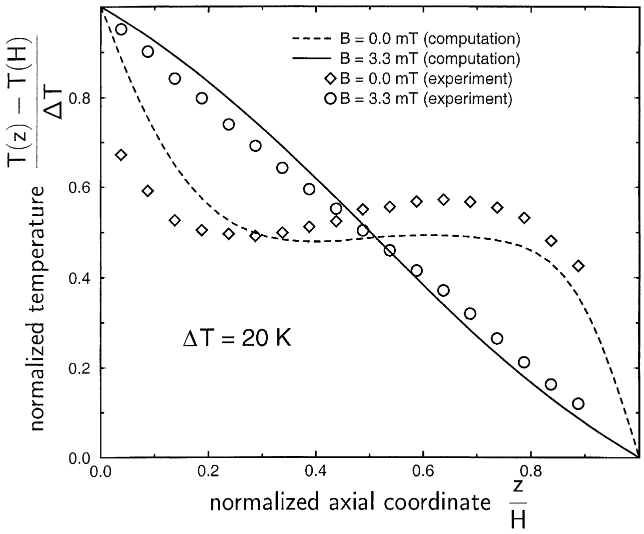

Figure 6.
Numerically and experimentally obtained temperature profiles (time-averaged) on the cylinder axis, for $\Delta T = 20\text{K}$, in normalized presentation, with (B_0= 3.3mT, $\omega = 2\pi \cdot 50\text{Hz}$) and without a rotating magnetic field

Source: Friedrich *et al*. (1999)

uncertainties like positioning of the temperature sensor and not completely ideal thermal boundary conditions in the set-up, and appear independently from the choice of the numerical grid.

With the results of calculations for the three-dimensional time-dependent flow in a cylinder with aspect ratio $\frac{H}{D} = 0.5$ (D=3.4cm) the different flow regimes that appear when increasing the magnetic field amplitude will now be illustrated ($\omega = 2\pi\cdot$ 50Hz, ΔT = 10K, if not stated otherwise). Time-dependent numerical temperature signals have been recorded at three different monitor points at $z = \frac{H}{3}$ and $r = R - 4\text{mm}$, which were azimuthally separated by 90° in order to study phase shifts between the signals. All horizontal sections through the cylinder in the following Figures will also be presented for $z = \frac{H}{3}$. Figure 7

Figure 7.
Velocity profile and isotherms for the aspect ratio 0.5 Rayleigh-Bénard configuration with ΔT =10K, in a vertical section, without rotating magnetic field. The isotherms are equally spaced (ΔT_{iso}= 1.1K). The maximum values of the cylindrical velocity components are: $v_{r,\max} = 5\,\frac{\text{mm}}{\text{s}}$, $v_{\varphi,\max} = 0\,\frac{\text{mm}}{\text{s}}$, $v_{z,\max} = 4\,\frac{\text{mm}}{\text{s}}$

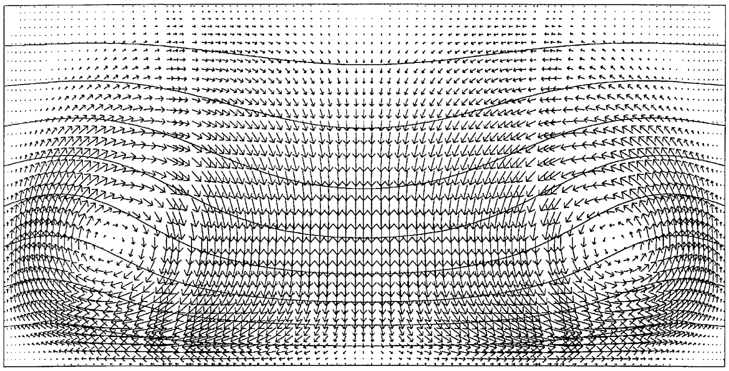

in a vertical section of the cylinder shows the purely buoyant flow for $B_0 = 0.0\text{mT}$, in this case an axisymmetric torus with velocity components only in the meridional plane. For other parameters also three-dimensional or even time-dependent buoyant patterns can be found, similar to previous numerical results for buoyancy driven convection in a cylindrical cavity (e.g. Crespo del Arco *et al.*, 1988); e.g. when enforcing buoyancy by increasing ΔT to $20K$, the axial symmetry is broken and one ends up in a temperature and flow pattern with wavenumber 2. This is shown in Figure 8 for a horizontal section of the cylinder.

When a small rotating magnetic field is applied, the basically azimuthal Lorentz force puts the fluid in rotation. Hybrid flow and temperature patterns appear as a mixture of the buoyant flow structures and the magnetically forced rotation, which are slowly proceeding in the azimuthal direction. At $\Delta T = 10\text{K}$, a rotating magnetic field of $B_0 = 0.6\text{mT}$ builds up a flow pattern with wavenumber 2, which is illustrated by a horizontal section in Figure 9. The corresponding temperature fluctuations at the three monitor points are shown in Figure 10. The slow procession of the temperature pattern causes regular large-scale fluctuations. The phase shift between the signals is also a sign for wavenumber 2.

When further increasing the amplitude of the magnetic field the regular, often sinusoidal, temperature fluctuations remain. In general, their frequency increases due to the increased rotational motion of the fluid. Moreover, separated by a very small transition regime where the three monitor signals show no phase shift, one may find a change in the wave number of the flow pattern. Remaining at $\Delta T = 10\text{K}$, a magnetic field of $B_0 = 1.5\text{mT}$ reveals a

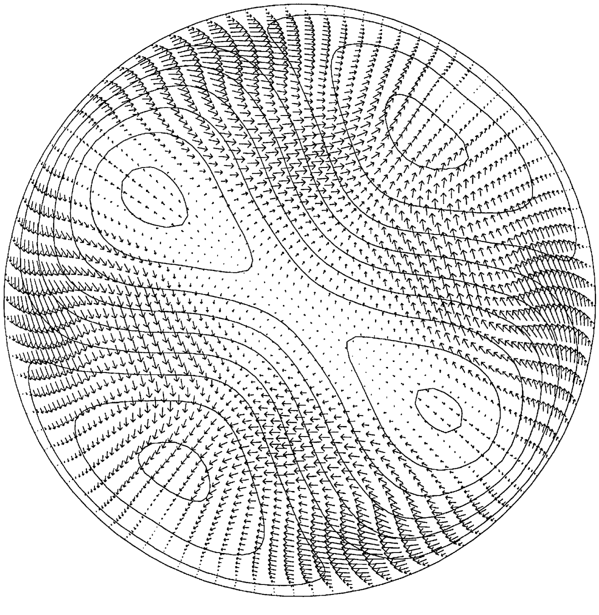

Figure 8. Velocity profile and isotherms for the aspect ratio 0.5 Rayleigh-Bénard configuration with $\Delta T = 20\text{K}$ in a horizontal section ($z = y_3 = \frac{H}{3}$), without rotating magnetic field. The isotherms are equally spaced ($\Delta T_{\text{iso}} = 1.05\text{K}$). The maximum values of the cylindrical velocity components are: $v_{r,\max} = 12\,\frac{\text{mm}}{\text{s}}$, $v_{\varphi,\max} = 12\,\frac{\text{mm}}{\text{s}}$, $v_{z,\max} = 14\,\frac{\text{mm}}{\text{s}}$

temperature pattern with wavenumber 1, as can be seen in the horizontal section in Figure 11. Accordingly, the phase shift between the temperature signals changes (Figure 12).

Beyond a certain threshold of the magnetic field (in this case at $B_0 = 2.0$mT) the forced rotation gains complete dominance over buoyancy and the flow is reduced to a mere rotation around the cylinder axis (see horizontal section for $B_0 = 4.5$mT in Figure 13), except for the secondary motion, which was illustrated in Figure 5 and Taylor-vortex-type instabilities that appear at the vertical cylinder wall for high magnetic fields (for the considered parameters at $B_0 \approx 5.0$mT) and result in irregular and non-correlated temperature fluctuations at the monitor points, with high frequency and small amplitude in comparison to the large-scale fluctuations coming from the pattern procession. Before the onset of these instabilities, however, the temperature fluctuations can be completely damped (for other parameters, e.g. a larger ΔT, they can at least be reduced significantly), resulting in the desired stabilization of the flow.

Similar flow regimes and flow transitions can be found for other system parameters. The stronger the buoyant forces (i.e. ΔT) are, the stronger must be the applied rotating magnetic field in order to achieve a sufficient damping of the temperature fluctuations. Observations that were made for aspect ratio 1.0 (Friedrich *et al.*, 1999) could be confirmed. The large-scale fluctuation regime was investigated in more detail in this study, numerically identifying changes in the wavenumber of the flow and temperature pattern, as well as the small transition area without phase shift in between wavenumber 2 and wavenumber 1.

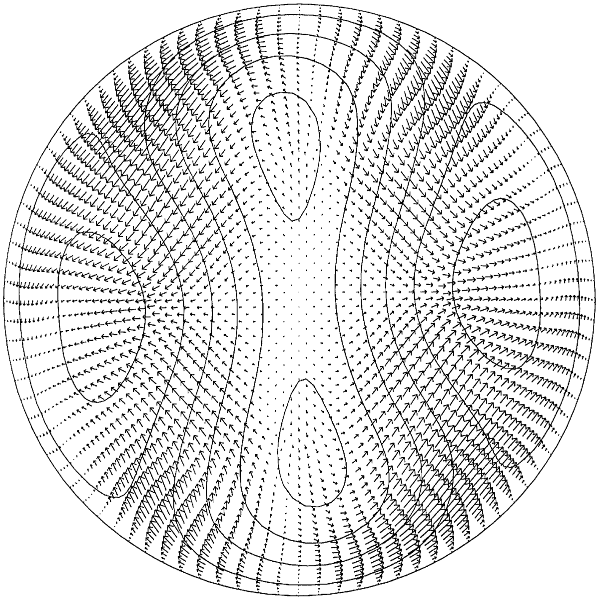

Figure 9.
Velocity profile and isotherms for the aspect ratio 0.5 Rayleigh-Bénard configuration with ΔT =10K in a horizontal section ($z = y_3 = \frac{H}{3}$), with a rotating magnetic field ($B_0 = 3.3$mT, $\omega = 2\pi \cdot 50$ Hz). The isotherms are equally spaced ($\Delta T_{\mathrm{iso}} = 0.53$K). The maximum values of the cylindrical velocity components are: $v_{r,\max} = 5\,\frac{\mathrm{mm}}{\mathrm{s}}$, $v_{\varphi,\max} = 6\,\frac{\mathrm{mm}}{\mathrm{s}}$, $v_{z,\max} = 8\,\frac{\mathrm{mm}}{\mathrm{s}}$

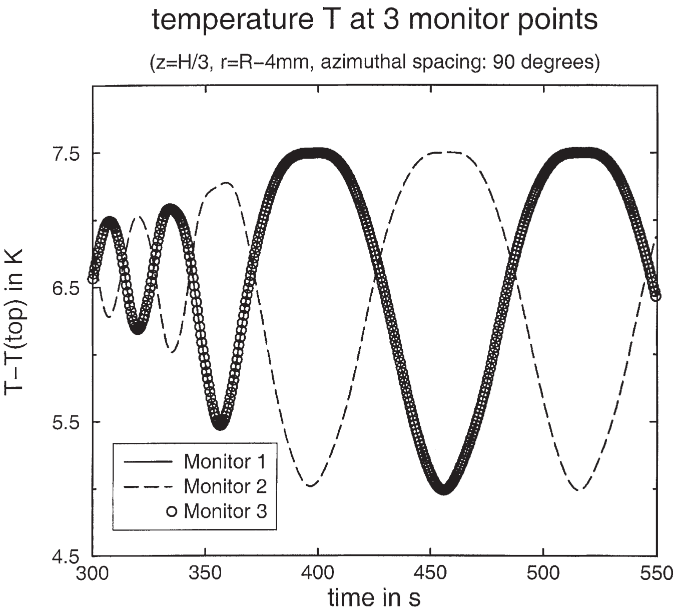

Note: From the phase shift between the signals it can be deduced that the flow and temperature pattern has wavenumber 2. This can also be seen in the horizontal section in Figure 9. Numerically starting from a state with the fluid at rest, the flow slowly builds up as soon as the buoyant and magnetic forces are active, ending up in regular temperature oscillations. In this special case, the transition from build-up to regular oscillations takes place at t ≈ 370s

Figure 10. Temperature signals at three monitor points at $z = y_3 = \frac{H}{3}$, $r = R - 4\text{mm}$, azimuthally separated by 90°.

4. Conclusions

A three-dimensional finite volume method was developed and presented to study the influence of rotating magnetic fields on fluid flow in a finite cylindrical conducting melt. The case without melt flow was tested by comparison with analytical solutions. The flows in typical cylindrical Rayleigh-Bénard configurations were studied under the action of a rotating magnetic field for cylinders with aspect ratios 0.5 and 1.0. The most important conclusion is that a relatively weak rotating magnetic field can have a significant effect on the flow configuration, resulting in a predominantly azimuthal flow and an efficient damping of disturbing temperature fluctuations resulting from time-dependent buoyant convection. Moreover, flattened isotherms provide a stabilized heat and mass transport in the axial direction. The interaction of buoyant and magnetic forces that act on the flow was investigated in detail, identifying several different flow regimes. We conclude that rotating magnetic fields offer a promising possibility to control flows in electrically conducting melts with benefits for application in crystal growth configurations.

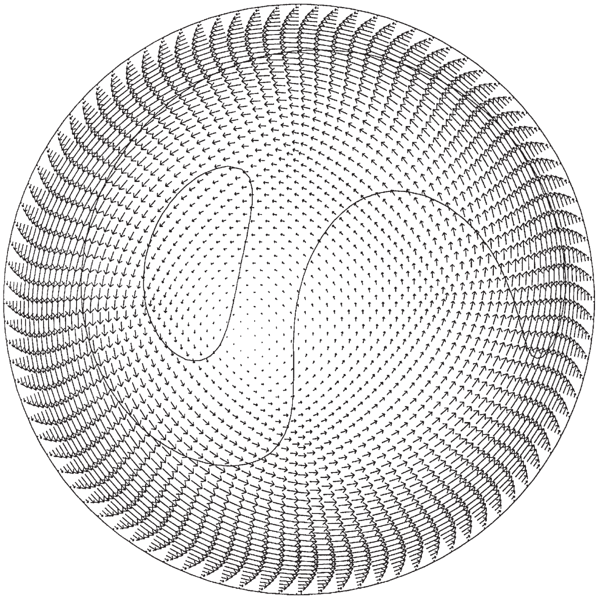

Figure 11.
Velocity profile and isotherms for the aspect ratio 0.5 Rayleigh-Bénard configuration with ΔT = 10K in a horizontal section ($z = y_3 = \frac{H}{3}$), with a rotating magnetic field (B_0 = 1.5mT, $\omega = 2\pi \cdot$ 50Hz).

Note: The isotherms are equally spaced (ΔT_{iso} = 0.53K). The maximum values of the cylindrical velocity components are:

$$v_{r,\max} = 2\,\frac{\text{mm}}{\text{s}},\ v_{\varphi,\max} = 6\,\frac{\text{mm}}{\text{s}},\ v_{z,\max} = 1\,\frac{\text{mm}}{\text{s}}$$

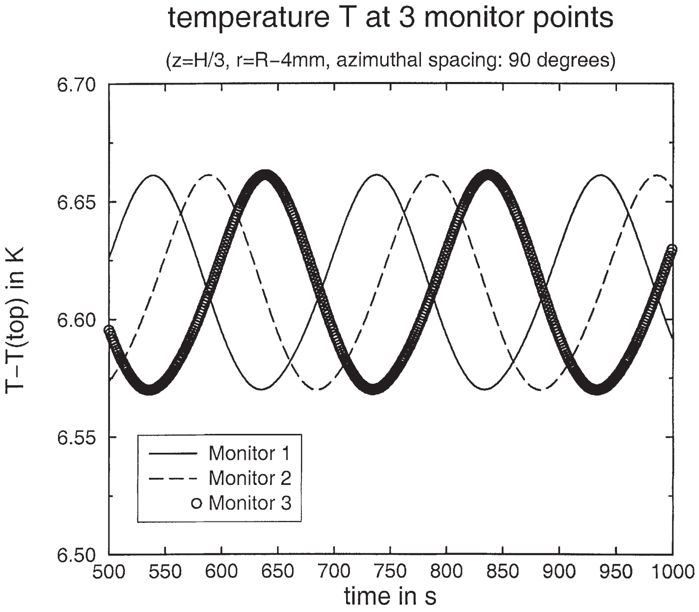

Figure 12.
Temperature signals at three points at $z = y_3 = \frac{H}{3}, r = R - 4\text{mm}$, azimuthally separated by 90°.

Note: From the phase shift between the signals it can be deduced that the flow and temperature pattern was wavenumber 1. This can also be seen in the horizontal section in Figure 11

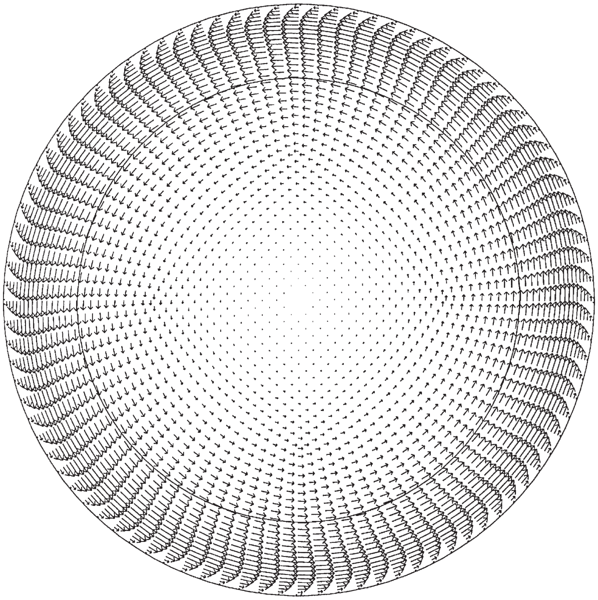

Note: The maximum values of the cylindrical velocity components are: $v_{r,\max} = 6\,\frac{\mathrm{mm}}{\mathrm{s}}$, $v_{\varphi,\max} = 29\,\frac{\mathrm{mm}}{\mathrm{s}}$, $v_{z,\max} = 3\,\frac{\mathrm{mm}}{\mathrm{s}}$

Figure 13. Velocity profile and isotherms for the aspect ratio 0.5 Rayleigh-Bénard configuration with ΔT = 10K in a horizontal section ($z = y_3 = \frac{H}{3}$), with a rotating magnetic field (B_0 = 1.5mT, $\omega = 2\pi\cdot$ 50Hz).

References

Abricka, M., Krümiņš, J. and Gelfgat, Yu.M. (1997), "Numerical simulation of MHD rotator action on hydrodynamics and heat transfer in single crystal growth processes", *J. Crystal Growth*, Vol. 180, pp. 388-400.

Barz, R.U., Gerbeth, G., Wunderwald, U., Buhrig, E. and Gelfgat, Yu.M. (1997), "Modelling of the isothermal melt flow due to rotating magnetic fields in crystal growth", *J. Crystal Growth*, Vol. 180, pp. 410-21.

Baumgartl, J. (1992), "Numerische und experimentelle Untersuchungen zur Wirkung magnetischer Felder in Kristallzüchtungsanordnungen", PhD Thesis, University Erlangen.

Crespo del Arco, E., Bontoux, P., Sani, R.L., Hardin, G. and Extrémet, G.P. (1988), "Steady and oscillatory convection in vertical cylinders heated from below. Numerical simulation of asymmetric flow regimes", *Adv. Space Res.*, Vol. 8, pp. (12)281-(12)292.

Dahlberg, E. (1972), *On the Action of a Rotating Magnetic Field on a Conducting Liquid*, AB Atomenergi, Sweden, Rep. AE-447.

Davidson, P.A. (1992), "Swirling flow in an axisymmetric cavity of arbitrary profile, driven by a rotating magnetic field", *J. Fluid Mech.*, Vol. 245, pp. 669-99.

Ferziger, J.H. and Perić, M. (1996), *Computational Methods for Fluid Dynamics*, Springer, Berlin.

Fischer, B., Friedrich, J., Kupfer, C., Müller, G. and Vizman, D. (1997), "Experimental and numerical analysis of the influence of a rotating magnetic field on convection in Rayleigh-Bénard configurations", *Proc. 3rd Int. Conf. on Transfer Phenomena in MHD and Electroconducting Flows*, Aussois, France, pp. 337-42.

Friedrich, J., Lee, Y.-S., Fischer, B., Kupfer, C., Vizman, D. and Müller, G. (1999), "Experimental and numerical study of Rayleigh-Bénard convection affected by a rotating magnetic field", *Physics of Fluids*, Vol. 11, pp. 853-61.

Gelfgat, Yu.M. and Priede, J. (1995), "MHD flows in a rotating magnetic field (a review)", *Magnetohydrodynamics*, Vol. 31, pp. 188-200.

Gelfgat, Yu.M., Gorbunov, L.A. and Kolevzon, V. (1993), "Liquid metal flow in a finite-length cylinder with a rotating magnetic field", *Exp. Fluids*, Vol. 15, pp. 411-16.

Gelfgat, Yu.M., Priede, J. and Sorkin, M.Z. (1991), "Numerical simulation of MHD flow induced by magnetic field in a cylindrical container of finite length", *Proc. Int. Conf. on Energy Transfer in MHD Flows*, Cadarache, France, pp. 181-6.

Gorbunov, L.A. and Kolevzon, V.L. (1993), "Flow of a conducting fluid in a rotating magnetic field", *Magnetohydrodynamics*, Vol. 28, pp. 380-5.

Johnston, W.C. and Tiller, W.A. (1961), "Fluid flow in the plane of the solid-liquid interface", *Trans. Met. Soc. AIME*, Vol. 221, pp. 331-6.

Kaiser, T. (1998), "Magnetohydrodynamische Effekte bei der Halbleiterkristallzüchtung", PhD thesis, University of Freiburg, Germany.

Leister, H.J. (1994), "Numerische Simulation dreidimensionaler, zeitabhängiger Strömungen unter dem Einfluß von Auftriebs- und Trägheitskräften", PhD thesis, University Erlangen.

Leister, H.J. and Perić, M. (1994), "Vectorized strongly implicit solving procedure for a seven-diagonal coefficient matrix", *Int. J. Num. Meth. Heat Fluid Flow*, Vol. 4, pp. 159-72.

Moffatt, H.K. (1965), "On fluid flow induced by a rotating magnetic field", *J. Fluid Mech.*, Vol. 22, pp. 521-8.

Moffatt, H.K. (1978), "Some problems in the magnetohydrodynamics of liquid metals", *Z. Angew. Math. Mech*, Vol. 58, pp. T65-T71.

Moreau, R. (1990), *Magnetohydrodynamics*, Kluwer Academic Publishers, Dordrecht.

Mößner, R. and Gerbeth, G. (1999), "Buoyant melt flows under the influence of steady and rotating magnetic fields", *J. Crystal Growth*, Vol. 197, pp. 341-54.

Müller, G. (1998), "Melt growth of semiconductors", *Materials Science Forum*, Vols. 276-77, pp. 87-108.

Patankar, S.V. (1980), *Numerical Heat Transfer and Fluid Flow*, McGraw-Hill, New York, NY.

Perić, M. (1985), "A finite volume method for the prediction of three-dimensional fluid flow in complex ducts", PhD thesis, University of London.

Priede, J. (1993), "Theoretical study of a flow in an axisymmetric cavity of finite length, driven by a rotating magnetic field", PhD thesis, University of Salaspils, Latvia.

Priede, J. and Gelfgat, Yu.M. (1997), "Numerical simulations of the MHD flow produced by a rotating magnetic field in a cylindrical cavity of finite length", *Magnetohydrodynamics*, Vol. 33, pp. 172-9.

Richardson, A.T. (1974), "On the stability of a magnetically driven rotating fluid flow", *J. Fluid Mech.*, Vol. 63, pp. 593-605.

Spitzer, K.-H., Dubke, M. and Schwerdtfeger, K. (1986), "Rotational electromagnetic stirring in continuous casting of round strands", *Metallurgical Transactions B*, Vol. 17B, pp. 119-31.

Stone, H.L. (1968), "Iterative solver of implicit approximations of multidimensional partial differential equations", *SIAM J. Num. Anal.*, Vol. 5, pp. 530-58.

Tomzig, E., von Ammon, W., Dornberger, E., Lambert, U. and Zulehner, W. (1999), "Challenges for economical growth of high quality 300mm CZ Si crystals", *Microelectronic Engineering*, Vol. 45, pp. 113-25.

Volz, M.P. and Mazuruk, K. (1996), "Flow transitions in a rotating magnetic field", *Exp. Fluids*, Vol. 20, pp. 454-9.